Effects of turbulence on the mean pressure field in the separated-reattaching flow above a low-rise building

Wu, C.-H.; Akon, A.F.; Kopp, Gregory

DOI:
10.1016/j.jweia.2017.09.013

Document Version
Peer reviewed version

Citation for published version (Harvard):
Wu, C-H, Akon, AF & Kopp, G 2017, 'Effects of turbulence on the mean pressure field in the separated-reattaching flow above a low-rise building', *Journal of Wind Engineering and Industrial Aerodynamics*, vol. 171, pp. 79-92. https://doi.org/10.1016/j.jweia.2017.09.013

Effects of turbulence on the mean pressure field in the separated-reattaching flow above a low-rise building

Chieh-Hsun Wu, Abul Fahad Akon, Gregory A. Kopp
Boundary Layer Wind Tunnel Laboratory, Faculty of Engineering,
University of Western Ontario, London, ON, Canada N6A 5B9

Correspondence: Gregory A. Kopp
Boundary Layer Wind Tunnel Laboratory, Faculty of Engineering, University of Western Ontario, London, ON, Canada N6A 5B9
Email: gakopp@uwo.ca; Tel: 519-661-2111 ext. 87572; Fax: 519-661-3339

Abstract

The effects of upstream turbulence in the atmospheric boundary layer flow on the mean surface pressure distribution within the separated flow above a typical low-rise building roof are investigated experimentally. Time-averaged Navier-Stokes equations are used to evaluate the pressure gradients from planar particle image velocimetry data. The pressure fields are reconstructed by integrating the pressure gradients using an analytic interpolation approach. This reconstruction approach is validated by successfully matching the reconstructed pressure to Bernoulli's equation along a streamline far from the body and with pressure measurements on the surface of the body. Through this process, the mean pressure field can be directly explained from the mean velocity and turbulence fields near the roof. For high turbulence intensity levels, the maximum suction coefficient on the roof surface was found to be increased. Such increased magnitudes are directly related to the reduced size of mean separation bubble in higher turbulence, more rapid variation of the velocity magnitude near the leading edge, and enhanced variation of the turbulence stresses. On the other hand, a higher rate of surface pressure recovery is found in the leeward portion of the separation bubble, which is mainly due to the more rapid variation of the turbulence stresses.

Keywords

Pressure integration methods; turbulent shear flows; separating-reattaching flows; building

aerodynamics.

Nomenclature

Cp	Pressure coefficient.
Cp_e	Estimated pressure coefficient.
Cp^*	Reduced pressure coefficient.
f	Frequency.
H	Height of the low-rise building model, $H = 8\,\text{cm}$.
I_u	Turbulence intensity of streamwise velocity component.
L_{ux}	Integral length scale of streamwise velocity component.
p	Pressure.
p_∞	Ambient static pressure.
r	Radial distance on the xz-plane, i.e., $r = \sqrt{x^2 + z^2}$.
S_{uu}	Auto-spectra of streamwise velocity component.
u	Streamwise velocity component (with direction parallel to x-coordinate).
$\mathbf{u}$	Velocity vector, $\mathbf{u} = u\mathbf{i} + v\mathbf{j} + w\mathbf{k}$.
u_H	Upstream streamwise velocity at roof height.
u_{ref}	Reference velocity.
w	Vertical velocity component with direction parallel to z-coordinate.
x	x-coordinate of the space.
x_r	Reattachment length of the mean separation bubble.
$\mathbf{x}$	Space vector. $\mathbf{x} = x\mathbf{i} + y\mathbf{j} + z\mathbf{k}$
z	Vertical coordinate of the space.
ν	Kinematic viscosity of air.
α	Coefficient associated with x-derivative of the analytic support, Φ.
β	Coefficient associated with z-derivative of the analytic support, Φ.
Φ	Analytic support.
ρ	Density of air.
σ	Support size of the radial analytic function Φ.
$\boldsymbol{\tau}$	Turbulence stress tensor with component $\tau_{ij} = \overline{u_i' u_j'}$
$\bar{a}$	Time average of a.
a'	Temporal fluctuation of a, i.e., $a' = a - \bar{a}$.
$\min(a)$	Minimum value of a.
$\max(a)$	Maximum value of a.

1. Introduction

Free-stream turbulence is known to affect the mean flow around two-dimensional (2D) rectangular prisms. For the separated and reattached flow near the leading edge, investigations over several decades (e.g., Kiya and Sasaki, 1984; Saathoff and Melbourne, 1997) have shown that increased free-stream turbulence intensity reduces the mean separation bubble length, x_r, on both the upper and lower surfaces. On the other hand, altering the length scale of turbulence has not been found to affect the length of the separation bubble as significantly as turbulence intensity (e.g., Hillier and Cherry, 1981; Nakamura and Ozono, 1987), at least over the range examined.

These findings have significant implications for the separated and reattached flow near a low-rise building roof, where large suctions can induce uplift failures in high winds. In order to investigate the influence of turbulence in the atmospheric boundary layer (ABL), Akon and Kopp (2016) conducted roof surface pressure measurements of a geometrically-scaled, low-rise building together with planar particle image velocimetry (PIV) measurements in a boundary layer wind tunnel. Near the height of the building, the turbulence intensity in their simulated ABLs ranged from 10% to 30% while the integral length scale ranged from 6 to 12 times of building height. Note that the turbulence intensity is defined as $I_u = \sqrt{\overline{u'u'}}/\overline{u}$, while the integral length scale is defined as $L_{ux} = \overline{u}\int_0^\infty \overline{u'(t)u'(t+t_*)}/\overline{u'u'}\,dt_*$, where $\overline{u}$ is the mean stream-wise velocity, u' is the fluctuating component, t denotes time and t_* is the time lag. The general effects of turbulence intensities and length scales on the mean reattachment length on the upper surface of the roof was found to be similar to the cases for 2D rectangular prisms. The distributions of mean pressure coefficients, $\overline{Cp}$, on the roof surface were found to be primarily dependent on the reattachment length, x_r, but also on the turbulence intensity. The minimum value of the mean pressure coefficient, $\min\left(\overline{Cp}\right)$, was found to asymptotically decrease for increased turbulence intensity. By further plotting the reduced mean pressure coefficients, $Cp^* = \left(\overline{Cp} - \min\left(\overline{Cp}\right)\right)/\left(1 - \min\left(\overline{Cp}\right)\right)$, as originally defined by Roshko and Lau (1965), against the normalized distance from the roof leading edge, x/x_r, they found that the mean pressure distributions beneath the separated flow are not self-similar because of the dependence on the

turbulence intensity, I_u. In particular, they found that the value of Cp^* decreases at the reattachment point, $x/x_r = 1$, for increased values of I_u, indicating that the pressure takes relatively longer to recover with respect to the reattachment point (which decreases for increased values of I_u).

With the capability of PIV measurements, our goal now is to look into the more detailed influences of ABL turbulence on the flow field variation near the roof. From the Navier-Stokes equations, the flow field can be directly connected to the pressure field so that the influence of turbulence on the pressure field can be examined. By defining the pressure coefficient, Cp, as

$$Cp = \frac{p - p_\infty}{0.5\,\rho u_{ref}^2}, \tag{1}$$

and normalizing the velocity vector, $\mathbf{u}$, by the reference velocity, u_{ref}, the gradient of the mean pressure coefficient can be written as:

$$\nabla\overline{Cp} = -2\left[\left(\frac{\overline{\mathbf{u}}}{u_{ref}}\right)\cdot\nabla\left(\frac{\overline{\mathbf{u}}}{u_{ref}}\right) + \nabla\cdot\left(\frac{\boldsymbol{\tau}}{u_{ref}^2}\right) - \frac{\nu}{u_{ref}}\nabla^2\left(\frac{\overline{\mathbf{u}}}{u_{ref}}\right)\right]. \tag{2}$$

Here ρ denotes the density of the air, p denotes the pressure, p_∞ is the ambient static pressure and ν is the kinematic viscosity. The overbars in Eq. (2) denote the time average, while $\boldsymbol{\tau}$ denotes the turbulent stress tensor with components $\tau_{ij} = \overline{u_i' u_j'}$ with the prime denoting a fluctuating component.

This Eulerian approach to pressure gradient evaluation, along with methods of pressure integration have been explored by many researchers and is recently reviewed by van Oudheusden (2013). The central difference scheme, which is of second order accuracy and relatively simple in operation, is usually used in determining the velocity gradients on the right hand side of Eq. (2) (e.g., Murai et al., 2007; de Kat and van Oudhuesden, 2012). On the side of pressure integration, however, greater attention is needed. Space-marching techniques for pressure integration are relatively straightforward and fast (e.g., Baur and Kőngeter, 1999; van Oudheusden et al., 2007). However, at times 'memory' effects of integrated results along the integration path can occur (e.g., de Kat et al. (2008)), which means the pressure integration can be path dependent with errors from either discretization or measurement (e.g., Sciacchitano and Wieneke, 2016) being accumulated along the integration path (Ettl et al., 2008). Because of these drawbacks for space-marching schemes, other types of optimization methods for pressure

integration may be preferable. The most common approach is to solve the Poisson equation for pressure with standard numerical techniques (e.g., Gurka et al., 1999; de Kat and van Oudheusden, 2012). Note that boundary conditions of mixed type, i.e., a combination of Dirichlet and Neumann, are required for solving Poisson equations (van Oudheusden, 2013). In addition to these techniques, algorithms in CFD have also been used to determine pressure from measured velocity data. For example, Jaw et al. (2009) calculated the pressure distribution through the SIMPLER algorithm, in which continuity is satisfied and no boundary conditions are required. In contrast to these methods, in the current work we are applying the analytic interpolation approach proposed by Ettl et al. (2008). The goal of this method is to keep the local details of integration while providing a globally optimized solution. This method has other advantages, such as no requirements for entire boundary conditions and the ability to remove bad gradient data.

An overview of this paper is as follows. The planar PIV and surface pressure measurements of the flow fields around a low-rise building under various terrain roughness conditions, as measured by Akon and Kopp (2016), are used as the input for analytic interpolation technique. Following a description of the method, the mean pressure fields are obtained from the measured mean velocity fields. The roof surface pressures estimated from velocity fields are then compared to the measurements. Effects of turbulence in the ABL on the mean roof surface pressure distributions are, hence, examined directly.

2. Atmospheric boundary layer (ABL) flow simulation with various terrain roughness conditions

Six upstream terrain conditions were used for generating the turbulent atmospheric boundary layer (ABL) flows. While the measurements are briefly reviewed here, full details can be found in Akon and Kopp (2016). These ABL turbulent flows are simulated in the high-speed test section of Boundary Layer Wind Tunnel II at the University of Western Ontario (UWO), which offers a fetch of 39 m for flow development and a cross-section of 3.36 m in width and 2.05 m in height at the test location. At the upstream end, three spires, with a height of 1.22 m and a base width of 0.1 m, are placed. Sets of roughness blocks are distributed along the floor between the upstream end and the test location. By altering the heights of the roughness blocks, three distinct

ABL turbulent flows, which are called 'Flat', 'Open' and 'Suburban' in this paper, are generated. By further placing a barrier of 0.38 m (15 inch) height immediately after the spires, along with the same sets of roughness blocks mentioned earlier, another three sets of ABL flow are generated with altered integral scales. In summary, the measurements were conducted with a total of six terrain roughness conditions. Three of them, with 15 inch barrier at the upstream end, are labelled as 'F15', 'O15'and 'S15' for Flat, Open and Suburban roughness distributions, respectively; the remaining three, without upstream barriers, are labelled as 'F0', 'O0' and 'S0', correspondingly.

In order to measure characteristic profiles of the simulated ABL turbulent flows, four-hole Cobra probes (TFI Inc., model no. 900) were used. The working principles for velocity measurements using these probes can be found on the manufacturer's website (TFI Inc., 2017). The Cobra probes used were calibrated by the manufacturer, which were verified by comparisons with Pitot-static probes in low turbulence flow. Akon (2017) assessed the measurement uncertainty as 2.3%. Vertical profiles of the mean longitudinal velocity component, $\overline{u}$, are normalized by the mean longitudinal velocity at the roof height, i.e., $\overline{u}/\overline{u}_H$, two of which are shown in Figures 1(a-b) as a function of normalized height, z/H. Here, z denotes the vertical distance from the wind tunnel floor and $H = 0.08\,\text{m}$ is the building height of the (geometrically-scaled) model. Near the roof, i.e., $z/H \le 3$, similar vertical distributions of $\overline{u}/\overline{u}_H$ can be found for the Flat and Open terrains (i.e., 'F0', 'F15', 'O0' and 'O15') while a significant increase of shear is observed in the Suburban terrains (i.e., 'S0' and 'S15'). The ratios of building height to roughness length, known as the Jensen number, are 540, 600, 290, 600, 56 and 71 for terrains 'F0', 'F15', 'O0', 'O15', 'S0' and 'S15' respectively, as reported by Akon and Kopp (2016). Figure 1(c) shows the vertical profiles for the turbulence intensities, $I_u = \sqrt{\overline{u'u'}}/\overline{u}$, in each of the six terrains. Clear increases in turbulence intensities can be observed for increased roughness along the wind tunnel floor. Adding the 15-inch barrier at the upstream end has less effect on turbulence intensity. Hence, the relative intensity of turbulence near the roof height can be a summarized as $I_{u,\text{F0}} \cong I_{u,\text{F15}} < I_{u,\text{O0}} \cong I_{u,\text{O15}} < I_{u,\text{S0}} < I_{u,\text{S15}}$, where the terrains are labelled in the subscripts.

The power spectral densities of the longitudinal velocity fluctuations were also obtained at

184 the roof height for the six terrains. Instead of using the typical normalization, $fS_{uu}/\overline{u'u'}$, for the
185 spectra, we have non-dimensionalized them as $fS_{uu}/\overline{u}^2$, where f denotes the frequency and
186 S_{uu} is the autospectral density. This normalization is similar to the conventional one but with
187 additional information on turbulence intensity, since $\int_{f=0}^{\infty} S_{uu}/\overline{u}^2\, df$ is in fact equal to I_u^2. So, the
188 clear increases of turbulence intensity due to increased roughness that are observed in Figure 1(c)
189 are reflected in the magnitude changes in the reduced spectra in Figure 1(d). In addition to the
190 magnitude of the fluctuations, the associated length scales can also be observed for the six
191 upstream turbulence conditions. The reduced spectra obtained from F15 and O15 generally shift
192 the F0 and O0 counterparts toward the larger length scale side (Figure 1(d)). However, S15
193 terrain not only produces more large scale turbulence but maintains the smaller scale turbulence
194 equivalent to S0, leading to total increase of turbulence intensity shown in Figure 1(c). Akon and
195 Kopp (2016) reported the ratios of integral length scales to building height, L_{ux}/H, as being 6,
196 8, 7, 13, 11 and 12 for terrains F0, O0, S0, F15, O15 and S15, respectively, where the integral
197 length scale is defined as $L_{ux} = \overline{u}\int_0^{\infty} \overline{u'(t)u'(t+t_*)}/\overline{u'u'}\, dt_*$. The vertical distributions of L_{ux} are
198 found to be nearly uniform for the region close to the roof. Hence, the terrains with the 15-inch
199 barrier at the upstream end produce turbulent flows of larger length scales as compared to
200 terrains without the barrier. Note that these ABL flows produced from the six sets of terrain
201 roughness are generally applicable for wind tunnel simulation of the real wind environment
202 (Akon and Kopp, 2016).
203
204

205 **3. PIV and pressure measurement on a low-rise building model**

206 The Time-Resolved Particle Image Velocimetry (TR-PIV) measurements, synchronized with
207 surface pressure measurements, were taken by Akon and Kopp (2016) on a 1/50 scaled model of
208 Texas Tech University's Wind Engineering Research Field Laboratory (WERFL) Building
209 (Levitan and Mehta, 1992). These data were utilized in the present study. The modelled
210 building has plan dimensions of 18.3 cm × 27.5 cm with a height of 7.8 cm (see Figure 2). Nine
211 pressure taps were placed along the centreline of the model roof surface to facilitate the pressure

measurements. The pressure coefficients have an absolute measurement uncertainty of about 0.1 on *Cp* values (Quiroga, 2006).

The TR-PIV system, used by Akon and Kopp (2016), uses two 1Mb Photron FASTCAM-1024 PCI CMOS cameras. A time delay of 85 micro-seconds was applied between the two images of a single image pair. The TR-PIV measurements of the velocity field (sampling frequency of 500 Hz) synchronized with roof-surface pressure measurements (sampling frequency of 1108 Hz) were taken for a duration of 160 seconds for each of the six upstream flow conditions. A detailed discussion on the TR-PIV system, and the synchronization of the pressure and velocity measurements can be found in Taylor et al. (2010). Interrogation windows of 32×32 pixels with 50% overlap were used during processing the PIV raw images in TSI Insight 4G utilizing an FFT cross-correlation algorithm. Standard cross-correlation algorithms have a spatial uncertainty of less than approximately 0.1 pixels (Huang et al., 1997). The final grid spacing between data points is $\Delta x = \Delta z = 0.2$ cm for upstream field of view (i.e., FOV 1 in Figure 2) and $\Delta x = \Delta z = 0.18$ cm for rooftop field of view (i.e., FOV 2 in Figure 2). The Cartesian coordinate system used in current analyse is also attached in Figure 2. A detailed explanation of the experimental procedure can be found in Akon and Kopp (2016).

The PIV data are compared to the Cobra probe data in Figures 1(a-b) for the mean profiles, and in Figure 1(c) for the turbulence intensity profiles. These figures indicate that there is an excellent match between the mean profiles, while there are differences in the turbulence intensities of up to 0.02 – 0.03, which can be explained by the measurement uncertainty.

4. Integration of planar pressure gradient data using the analytic interpolation technique

The analytic interpolation technique proposed by Ettl et al. (2008) for surface reconstruction is explained and applied for integrating mean pressure gradient data in this section. The Navier-Stokes equations, represented in Eq. (2), are used to determine the mean pressure gradient using planar PIV measurement data. For wind normal to the building and a measurement plane on the centerline, the mean flow field can be treated as symmetric and, hence, the gradients associated with out-of-plane component are negligible. The exact components used in Eq. (2) for evaluation of mean pressure gradient are:

242 $$\frac{\partial \overline{Cp}}{\partial x} = -2\left[\frac{\overline{u}}{u_{ref}}\frac{\partial}{\partial x}\left(\frac{\overline{u}}{u_{ref}}\right) + \frac{\overline{w}}{u_{ref}}\frac{\partial}{\partial z}\left(\frac{\overline{u}}{u_{ref}}\right) + \frac{\partial}{\partial x}\left(\frac{\overline{u'u'}}{u_{ref}}\right) + \frac{\partial}{\partial z}\left(\frac{\overline{u'w'}}{u_{ref}}\right) - \frac{\nu}{u_{ref}}\left(\frac{\partial^2}{\partial x^2}\left(\frac{\overline{u}}{u_{ref}}\right) + \frac{\partial^2}{\partial z^2}\left(\frac{\overline{u}}{u_{ref}}\right)\right)\right] \quad (3a)$$

243 $$\frac{\partial \overline{Cp}}{\partial z} = -2\left[\frac{\overline{u}}{u_{ref}}\frac{\partial}{\partial x}\left(\frac{\overline{w}}{u_{ref}}\right) + \frac{\overline{w}}{u_{ref}}\frac{\partial}{\partial z}\left(\frac{\overline{w}}{u_{ref}}\right) + \frac{\partial}{\partial x}\left(\frac{\overline{u'w'}}{u_{ref}}\right) + \frac{\partial}{\partial z}\left(\frac{\overline{w'w'}}{u_{ref}}\right) - \frac{\nu}{u_{ref}}\left(\frac{\partial^2}{\partial x^2}\left(\frac{\overline{w}}{u_{ref}}\right) + \frac{\partial^2}{\partial z^2}\left(\frac{\overline{w}}{u_{ref}}\right)\right)\right] \quad (3b)$$

244 On the right-hand side of Eq. (3), the 1st and 2nd terms are associated with the mean convection,
245 the 3rd and 4th terms are associated with turbulence, and the 5th and 6th terms are associated with
246 viscous stresses.

247 The analytic interpolation approach developed by Ettl et al. (2008) offers an effective tool for
248 topological surface reconstruction by integrating measured gradient data. Because the
249 differential momentum equation offers gradient information of pressure, as shown in Eq. (3), the
250 reconstruction method of Ettl et al. (2008) will be applicable to pressure reconstruction. In this
251 approach, the estimated pressure coefficient, Cp_e, at location $\mathbf{x}$ is assumed as a linear spatial
252 superposition of analytic functions, i.e.,

253 $$Cp_e(\mathbf{x}) = \sum_{j=1}^{N}\left[\alpha_j \frac{\partial}{\partial x}\Phi(\mathbf{x}-\mathbf{x}_j) + \beta_j \frac{\partial}{\partial z}\Phi(\mathbf{x}-\mathbf{x}_j)\right], \quad (4)$$

254 where α_j and β_j are the appropriate coefficients for the x and z derivatives of analytic support
255 centred at the *j*-th grid point, respectively; N denotes total number of grid points. Wenland's
256 function was selected by Ettl et al. (2008), and is also used here for the analytic support, Φ.
257 This function is symmetric about its centre and resembles a bell-shaped surface for the radial
258 distance $r \le 1$ and is zero for regions of $r > 1$, i.e.,

259 $$\Phi(r) = \begin{cases} \frac{1}{3}(1-r)^6(35r^2+18r+3) & \text{for} \quad r \le 1 \\ 0 & \text{for} \quad r > 1 \end{cases} \quad \text{with} \quad r = \sqrt{x^2+z^2}\,. \quad (5)$$

260 The support size, which is denoted as σ, describes the range of influence of the radial support
261 Φ. As can be seen in Eq. (5), the support size is unity for the original Wenland's function.
262 Adjustment of the support size may be needed in order to render smooth integration results for
263 various grid spacings. Such adjustment can be simply achieved by replacing original grid
264 location, $\mathbf{x}$, in Eq. (4) by the normalized one, $\mathbf{x}/\sigma$. Thus, the $Cp_e(\mathbf{x})$ in Eq. (4) is directly
265 related to *j*-th support if $|\mathbf{x}-\mathbf{x}_j| \le \sigma$, while supports outside the influence region can be
266 neglected in Eq. (4). In order to determine the coefficients α and β, the gradient of Cp_e

represented by Eq.(4) is taken at grid point $\mathbf{x}_i$ and matched with the measured gradient data obtained from the Navier-Stokes equations, Eq.(3), such that

$$\underbrace{\begin{bmatrix} \frac{\partial^2}{\partial x^2}\Phi(\mathbf{x}_i-\mathbf{x}_j) & \frac{\partial^2}{\partial x\partial z}\Phi(\mathbf{x}_i-\mathbf{x}_j) \\ \frac{\partial^2}{\partial x\partial z}\Phi(\mathbf{x}_i-\mathbf{x}_j) & \frac{\partial^2}{\partial z^2}\Phi(\mathbf{x}_i-\mathbf{x}_j) \end{bmatrix}}_{\mathbf{A},\ 2N\times 2N} \underbrace{\begin{bmatrix} \alpha_j \\ \beta_j \end{bmatrix}}_{\mathbf{c},\ 2N\times 1} = \underbrace{\begin{bmatrix} \frac{\partial}{\partial x}\overline{Cp}(\mathbf{x}_i) \\ \frac{\partial}{\partial z}\overline{Cp}(\mathbf{x}_i) \end{bmatrix}}_{\mathbf{d},\ 2N\times 1}. \tag{6}$$

Once the linear system described in Eq.(6) is established, the coefficients can be solved by matrix inversion.

There are a few notes regarding the application. First, since the integration scheme is based on gradient data, the integrated values resulting from Eq.(4) only offer information of relative difference. Therefore, it is necessary to specify a constant of integration at a specified location within the domain of measurement. Second, if a normalized grid location, $\mathbf{x}/\sigma$, is used in Eq. (4), the measured gradient data must be pre-multiplied by σ before putting into vector $\mathbf{d}$ in Eq.(6), in order to account for the chain rule.

The current interpolation method allows users to treat bad data points with two options because of the advantages of the mathematical nature of Eq. (4). Within the measurement plane, assume that there are bad gradient data points scattered at locations $\mathbf{x}_b$, which have a total number of N_b. The first option is to exclude the radial basis supports located at $\mathbf{x}_b$ in Eq. (4) but keep full gradient data in $\mathbf{d}$ in Eq. (6). In this case, $\mathbf{A}$ becomes a non-square matrix of dimension $2N\times 2(N-N_b)$ and $\mathbf{d}$ is still a vector of dimension $2N\times 1$. Then, a least-squares method can be used to solve for the coefficient vector $\mathbf{c}$ in Eq. (6), as mentioned in Ettl et al. (2008). The second option is to remove both the supports at $\mathbf{x}_b$ in Eq. (4) and bad gradient data in vector $\mathbf{d}$ in Eq. (6). The corresponding dimensions of matrices $\mathbf{A}$ and $\mathbf{d}$ have sizes of $2(N-N_b)\times 2(N-N_b)$ and $2(N-N_b)\times 1$, respectively, in this case. Therefore, direct matrix inversion can be used again to solve the coefficient vector. The reconstruction at bad gradient data locations can then be treated as extrapolation by simply evaluating $Cp_e(\mathbf{x}_b)$ in Eq. (4). Interested readers are referred to Ettl et al. (2008) for more useful techniques for application.

A review of the details used in current pressure integration is as follows. Once the mean velocities and turbulence stresses are captured from the two PIV FOV's in Figure 2, they are normalized by reference velocity, u_{ref}, for calculation of Eq. (3). The reference velocity used throughout this paper is defined as mean streamwise velocity at roof height and an upstream location where no influences of building are expected, i.e., $u_{ref} = \overline{u}_H$. (It should be noted that the region of influence is at least 2*H* upstream of the building, which is not captured by the images in Figure 3.) The central difference scheme is applied to calculate the pressure gradient vectors according to differential momentum in Eq. (3). Bad pressure gradient data are identified and removed in the reconstruction process if the magnitude is two times larger or the direction deviates 120˚ from the averaged value obtained from its eight immediate neighbors. The bad pressure gradient data are mainly located near the model surface due effects of laser reflection. The maximum number of the bad data points is fewer than 2% of the data points within the two fields of view. The size of the analytic support is chosen to be about 14 times that of the PIV data grid spacing in order to render reconstruction smoothness.

The integration process is first conducted for FOV 1 by using the gradient information measured in this FOV. The mean pressure is assumed to be the same as the ambient value, i.e., $\overline{Cp} = 0$, at the upstream, higher corner of FOV 1, i.e., $\{x = -1.5H, z = 1.75H\}$. This assumption is based on zero pressure gradient in the vertical direction in boundary layer equation (e.g., Wilcox, 2007) for upstream flow where the interference of the model is minimal (e.g., Peren et al., 2015). Following a similar approach but assuming an arbitrary initial integration constant, the pressure field can also be integrated for FOV 2. The reconstructed pressures in FOV 2 are then adjusted by an integration constant such that the difference of the area-averaged pressures within the overlap region between FOV's 1 and 2 (see Figure 2) is zero. Note that such procedure in fact minimizes the difference of integrated pressures within the overlapped region between FOV's 1 and 2 (Ettl et al., 2008).

5. Results and discussion

5.1. Convection terms

Planar PIV measurements were conducted near the building roof under the six upstream terrain conditions mentioned in Section 2. Figure 3 shows the ratio of the mean velocity magnitude, $|\overline{\mathbf{u}}|$, to a reference velocity, u_{ref}, for all six terrains. Generally, a speed-up ratio of about 1.4 can be found when comparing the mean upstream velocity at the roof height, and about 0.5H upstream of the building, to the velocity above the top of the roof on the same streamline. Low velocities can be found within the stagnation region in front of the wall and in the recirculation region above the roof. The contribution of the convection terms to the pressure gradient in the Navier-Stokes equations, i.e., the 1st and 2nd terms on the right-hand side of Eq. (3), is shown in Figure 4 for all six upstream terrain conditions. Generally, the gradient vectors are found to radiate from the windward corner, with the magnitudes being the largest near the leading edge and reduced above the mean separation bubbles (which are also shown in Figure 4). Over the regions farther away from the leading edge and within the separation bubbles, relatively small gradient vectors can be observed.

As already noted by Akon and Kopp (2016), the size of separation bubbles is much more sensitive to the intensity than the scale of the upstream turbulence, being smaller for greater values of turbulence intensity. Their observation can be easily verified by reviewing the turbulence intensities in Figure 1(c) and the mean separation bubbles in Figure 4. Because the curvature of the streamlines increases as the size of separation bubbles is reduced, the convection-contributed pressure gradients above the separation bubbles are intensified for rougher terrains. The terrain effects on relative mean velocity magnitude (see Figure 3) are not significant in general, although details of velocity variation near the leading edge are different when comparing the results in Figure 3 for terrains ‘F0’ and ‘S15’. Lower velocity magnitude variation near the leading edge can be found for terrain ‘F0’ while higher variation can be observed for terrain ‘S15’. The more rapid spatial variations of velocity magnitude increases the convection-contributed pressure gradients as well, so that the pressure gradients of terrain ‘S15’ are larger than that in terrain ‘F0’ near the leading edge (see Figure 4).

5.2. Turbulence terms

The three distinct components of turbulence stress tensors, $\overline{u'u'}$, $\overline{w'w'}$ and $\overline{u'w'}$, are normalized by reference velocity and shown respectively in Figures 5, 6 and 7. Once these turbulence stresses are measured, the turbulence contribution to the mean pressure gradient vectors, which is shown in Figure 8, can be obtained by evaluating the 3rd and 4th terms of Eq. (3). For the distribution of $\overline{u'u'}/u_{ref}^2$ **,** shown in Figure 5, maximum values are found to coincide with the shear layer region while decreasing values can be found for the regions away from the shear layers. By further comparing Figure 5 to Figures 6 and 7, it is observed that the $\overline{u'u'}$ component dominates the turbulence stress tensor, with maximum magnitudes around 4 times that of the other two. Hence, according to Eq. (3a), the turbulence-contributed pressure gradient vectors generally radiate from the shear layer in a nearly horizontal direction. For the distribution of $\overline{w'w'}/u_{ref}^2$ shown in Figure 6, larger magnitudes are found over the leeward half of the separation bubbles. The spatial variation of $\overline{w'w'}/u_{ref}^2$ is responsible for the pressure gradients in the vertical direction, according to Eq. (3b). For the distribution of $\overline{u'w'}/u_{ref}^2$ shown in Figure 7, a spatial migration of the positive peaks near the roof leading edge to the negative peaks over the leeward half of the separation bubbles can be found. According to Eq. (3), the vertical gradient of $\overline{u'w'}/u_{ref}^2$ is associated with the horizontal pressure gradient while the horizontal gradient of $\overline{u'w'}/u_{ref}^2$ is associated with the vertical pressure gradient.

The effects of upstream terrain conditions on the turbulence-contributed pressure gradients are described here. As shown in Figure 5, the maximum values of $\overline{u'u'}/u_{ref}^2$ increase as the intensity or length scale of the upstream turbulence increases. However, the influence of turbulence intensity is more significant than length scale. In particular, increasing $(I_u)^2$ in the upstream flow by a factor of four (i.e., doubling the turbulence intensity upstream) doubles the maximum values of $\overline{u'u'}/u_{ref}^2$ (or, taking the square root, the turbulence intensity above the roof by 40%; compare the Flat and Suburban terrains in Figure 5), while doubling L_{ux} only increase the maximum $\overline{u'u'}/u_{ref}^2$ by around 20% (or a 10% increase in the intensity above the roof; see terrains with and without the 15-inch barrier in Figure 5). For the $\overline{u'w'}/u_{ref}^2$ distribution shown in Figure 7, higher positive peak values are found for higher upstream turbulence intensity, while

negative peak values appear to be mostly independent from the terrain effects. However, the distances between the high and low peak values of $\overline{u'w'}/u_{ref}^2$ shrink as the sizes of separation bubbles reduce. For the distribution of $\overline{w'w'}/u_{ref}^2$ shown in Figure 6, reduced effects of the upstream terrain conditions can be observed. As a result of these variations, larger turbulence-contributed pressure gradients can be found for higher upstream turbulence intensities, for regions near the shear layers and roof surface, as shown in Figure 8. The effects of the turbulence length scales are observed to be less significant.

5.3. Total pressure gradients

For high Reynolds number flow, the viscosity contribution is relatively small (e.g., van Oudheusden et al., 2007). The contribution of the viscosity terms to the final integrated pressures are less than 1% for all the cases with the current measurements. By summing the contributions of convection, turbulence and viscosity in the Navier-Stokes equations, the total gradient of $\overline{Cp}$ can be obtained, and is shown in Figure 9 for each of the six terrains.

By assuming that the viscosity contribution is negligible, the vector contributions of the convection-contributed pressure gradient, $\left(\nabla\overline{Cp}\right)_{\text{conv}}$, and turbulence-contributed pressure gradient, $\left(\nabla\overline{Cp}\right)_{\text{turb}}$, to the total pressure gradient, $\left(\nabla\overline{Cp}\right)_{\text{total}}$, are schematically shown in Figure 10(a). In order to quantify the contributions, the projections of each term onto the total gradient are normalized by the magnitude of total gradient. For example, the vector contribution of the convection term can be formulated as follows:

$$\frac{\left|\left(\nabla\overline{Cp}\right)_{\text{conv}}\right|\cos\theta_{\text{conv}}}{\left|\nabla\overline{Cp}_{\text{total}}\right|}=\frac{\left(\nabla\overline{Cp}\right)_{\text{conv}}\cdot\left(\nabla\overline{Cp}\right)_{\text{total}}}{\left|\nabla\overline{Cp}_{\text{total}}\right|^2}, \tag{7}$$

where θ_{conv} is the angle between $\left(\nabla\overline{Cp}\right)_{\text{conv}}$ and $\left(\nabla\overline{Cp}\right)_{\text{total}}$, as defined in Figure 10(a). For the convenience of calculation, the vector contribution defined on the left-hand side of Eq. (7) can be represented as the inner product between $\left(\nabla\overline{Cp}\right)_{\text{conv}}$ and $\left(\nabla\overline{Cp}\right)_{\text{total}}$, as shown on the right-hand side of the same equation.

Preliminary calculation of the vector contribution using Eq. (7) shows similar pattern for all six upstream terrain conditions. Hence, only the results obtained from terrain O15 are shown here. As can be clearly seen in Figure 10(b), the convection term governs the total pressure gradient in the region above the separation bubbles and away from the building surface, for more than 90% of the total. On the other hand, the turbulence contribution shown in Figure 10 (c) governs the region within the separation bubbles, with maximum contribution of more than 90% near the roof surface along the leeward side of the separation bubbles.

5.4. Integrated pressure field

The analytic interpolation technique introduced in Section 4 is applied to integrate the total mean pressure gradients shown in Figure 9. The reconstructed $\overline{Cp}$ fields are shown in Figure 11 for the six terrain conditions. Smooth distributions of the integrated $\overline{Cp}$'s can be observed for all terrains, with the lowest negative values centered at the windward portion of the mean separation bubbles (see Figure 4). For locations far upstream of the building, relatively little variation of integrated pressures can be observed. Hence, by assuming that the pressure at an upstream point is equivalent to the ambient pressure, Bernoulli's equation, i.e.,

$$\overline{Cp}_{\text{roof top}} = \overline{Cp}_{\text{upstream}} + \frac{\left|\overline{\mathbf{u}}_{\text{upstream}}\right|^2}{u_{ref}^2} - \frac{\left|\overline{\mathbf{u}}_{\text{roof top}}\right|^2}{u_{ref}^2}, \tag{8}$$

can also be applied to evaluate the pressure along the streamlines and, therefore, serve as a crosscheck for the integrated results. In Eq. (8), $\overline{Cp}_{\text{upstream}}$ and $\overline{\mathbf{u}}_{\text{upstream}}$ denote, respectively, the mean pressure coefficients and velocity at an upstream location for the selected streamline, while $\overline{Cp}_{\text{roof top}}$ and $\overline{\mathbf{u}}_{\text{roof top}}$ denote, respectively, the mean pressure coefficient and velocity at a downstream location above the roof on the same streamline. Two streamlines are selected, in terrains 'F0' and 'S15', for this purpose (see Figures 8 and 11): The upper streamline starts at an upstream point near $\{x = -H; \text{y} = 1.375H\}$ while the lower one starts at an upstream point near $\{x = -H; y = 0.75H\}$. Figure 12 shows the comparison of Bernoulli-estimated $\overline{Cp}$'s to the integrated results extracted from the upper and lower streamlines in Figure 11. Good agreement of $\overline{Cp}$'s can be found between Bernoulli's estimations and integrated results for the upper

streamlines under the two selected terrain conditions. Such agreement manifests the applicability of the analytic interpolation technique for pressure reconstruction introduced in Section 4. However, for the lower streamlines in both terrains, Bernoulli's equation begins to undershoot the suction at $\{x/H \approx 0.25\}$ and continues accumulating the underestimation for the rest of downstream region. Such accumulating underestimation of Bernoulli's equation is due to the absence of the turbulence-contributed pressure gradients near the separated shear layers. By reviewing the sub-plots in Figure 8 for terrains 'F0' and 'S15', both of the lower streamlines are found to enter the region of large turbulence-contributed pressure gradients near $\{x/H \approx 0.25\}$. Because these turbulence-contributed pressure gradient vectors point in the direction opposite to the flow direction, the missing accumulation of these vectors along the positive flow direction leads to an underestimation of Bernoulli-estimated $\overline{Cp}$'s along the lower streamlines.

5.5. Surface pressures

The mean roof surface pressure coefficients measured by Akon and Kopp (2016) are shown in Figure 13 for six upstream terrain conditions and compared to the integrated $\overline{Cp}$'s extracted from a horizontal line near the roof height in Figure 11. As the upstream turbulence intensity increases, progressive variations of the $\overline{Cp}$ distributions can be observed in the roof surface pressure measurements. For terrains producing lower turbulence intensity, the $\overline{Cp}$ distributions resemble a plateau for the windward portion of the separation bubbles. As the upstream turbulence intensity increases, the plateau reduces to a prominent peak as a result of reduced size of the separation bubble. The minimum $\overline{Cp}$ can also be found to gradually decrease as the upstream turbulence intensity increases (Akon and Kopp, 2016). For example, the $\min(\overline{Cp}) = -0.9$ is observed for roof height $I_u = 13\%$ (see Figure 1 (b)) while $\min(\overline{Cp}) = -1.3$ is observed for roof height $I_u = 27\%$. However, as the distance from the leading edge increases, these minimum $\overline{Cp}$'s gradually recover to a common value of $\overline{Cp} = -0.2$. Hence, higher rates of pressure recovery can be found for the rougher terrains that produce higher turbulence intensities. As discussed in the Introduction, because the $\overline{Cp}$ distributions are strongly

dependent on the sizes of the separation bubbles, Akon and Kopp (2016) also examined the universality of the mean pressure distributions by plotting Roshko and Lau's (1965) reduced form of mean pressure coefficients, i.e.,

$$Cp^* = \frac{\overline{Cp} - \min\left(\overline{Cp}\right)}{1 - \min\left(\overline{Cp}\right)}, \tag{9}$$

against reduced distance, x/x_r. Here Cp^* denotes the reduced pressure coefficients and x_r denotes the reattachment length. From the results shown in Figure 14, Akon and Kopp (2016) found that, although the minimum mean pressures generally locate at $x/x_r = 0.25$ for these six terrains, the distribution of mean pressure coefficients is not self-similar.

The reconstructed field of $\overline{Cp}$'s are extracted from a horizontal line near roof height and compared to the roof surface measurements in Figure 13. Good agreement between the results obtained from the Navier-Stokes equations and the roof surface measurement can be observed for all six terrains, with maximum deviations in the magnitudes of $\max\left(\left|\Delta\overline{Cp}\right|\right)$ being less than 0.1. This is consistent with the measurement uncertainty of the surface pressure measurements of about 0.1 (Quiroga, 2006). Hence, the variation in the mean pressure coefficients observed from surface measurements for the six terrains can be observed in the integrated results as well.

As the upstream turbulence intensity increases, the minimum $\overline{Cp}$ obtained from integration also decreases (see Figures 11 and 13). By reviewing what has been discussed so far, for the gradient fields of the mean pressures (i.e., Figure 9), the decreasing minimum mean pressure is due to the increased pressure gradient obtained from both the convection (Figures 4 and 10(b)) and turbulence (Figures 8 and 10 (c)) terms in the Navier-Stokes equations of Eq. (3). Higher rates of pressure recovery can be found in the integrated results as well. However, the turbulence terms govern the pressure recovery for the region just above the roof (see Figures 8 and 10(c)) and higher turbulence-contributed pressure gradients can be found in this region for the rougher terrains that produce higher turbulence intensities. These increased pressure gradients, which lead to both the decreased minimum value and higher recovery rate of mean pressure, can be further linked back to the flow fields. As mentioned earlier, the increased convection-contributed pressure gradient is attributed to the reduced size of separation bubble (Figure 4) and more rapid spatial variation of velocity magnitude near the leading edge (Figure 3). On the other

hand, the increased turbulence-contributed pressure gradients are attributed to the increased spatial variation of $\overline{u'u'}/u_{ref}^2$ in Figure 5 and $\overline{u'w'}/u_{ref}^2$ in Figure 7. The summary of these effects for both the mean velocity and turbulence fields explains the variation of the $\overline{Cp}$ distribution on the roof shown in Figures 13 and 14. However, the turbulence-induced pressure gradients are not large enough to allow the reduced pressure coefficient distribution to be self-similar (see Figure 14). As a result, the reduced pressure coefficient of Eq. (9) has a smaller magnitude at the mean reattachment point, $x/x_r = 1$ for higher turbulence flows.

6. Conclusions

The effects of the atmospheric boundary layer (ABL) turbulence intensity and length scales on the mean separated and reattached flow, and roof surface pressure were examined by Akon and Kopp (2016). The goal of the current work is to extend the understanding of their observations by further linking the velocity and turbulence fields to the pressure fields. The main contributions and findings are summarized as follows.

(i) The Navier-Stokes equations are used to determine the gradient vectors of the mean pressure field from the planar PIV data. The convection-contributed pressure gradients are identified by evaluating the terms associated with mean velocities in the Navier-Stokes equations. The turbulence-contributed pressure gradients, on the other hand, are identified by terms associated with the Reynolds stresses. Effects of upstream turbulence on both of the convection- and turbulence-contributed pressure gradients can, hence, be examined.

(ii) In order to obtain the pressure field from the velocity field, the analytical interpolation technique of Ettl et al. (2008) is applied. The reconstructed pressure fields match Bernoulli's equation well along a streamline away from the body and direct pressure measurement on the surface of the body. Hence, the evaluation of pressure gradient using the Navier-Stokes equations and the corresponding pressure integration technique are validated.

(iii) Akon and Kopp (2016) found that the minimum mean roof surface pressure coefficient, $\min\left(\overline{Cp}\right)$, decreases for increased upstream turbulence intensity. In the current work, these

decreasing $\min(\overline{Cp})$'s are directly related to both increased convection- and turbulence-contributed pressure gradients over the windward region of the mean separation bubbles.

(iv) As the upstream turbulence intensity increases, a more rapid pressure recovery can be found for the portion of roof surface on the leeward side of the location of $\min(\overline{Cp})$. Such increased surface pressure recovery rates are mainly due to the increased turbulence-contributed pressure gradients near the roof surface. However, the rate of recovery is not sufficiently high such the normalized pressure distribution is not self-similar.

Acknowledgements

This work was funded by the Natural Sciences and Engineering Research Council (NSERC) of Canada under the Collaborative Research and Development (CRD) program and by the Institute for Catastrophic Loss Reduction (ICLR).

References

Akon, A. F., Kopp, G. A., 2016. Mean pressure distributions and reattachment lengths for roof separation bubbles on low-rise buildings. J. Wind Eng. Ind. Aerodyn. 155, 115-125. DOI: 10.1016/j.jweia.2016.05.008

Akon, A.F., 2017, Effects of turbulence on the separating-reattaching flow above surface-mounted, three-dimensional bluff bodies. PhD thesis, The University of Western Ontario.

Baur, T., Kőngeter, J., 1999. PIV with high temporal resolution for the determination of local pressure reductions from coherent turbulent phenomena. In: 3rd Int. Workshop on Particle Image Velocimetry (Santa Barbara, USA, Sep. 16-18, 1999), 671-676.

de Kat, R., van Oudheusden, B. W., Scarano, F., 2008. Instantaneous planar pressure field determination around a square-section cylinder based on time-resolved stereo-PIV. In: 14th Int Symp. on Applications of Laser Techniques to Fluid Mechanics (Libson, Portugal, Jul. 7-10, 2008). http://ltces.dem.ist.utl.pt/lxlaser/lxlaser2008/programme.asp (Last date of access: Sep 1, 2017)

de Kat, R., van Oudheusden, B. W., 2012. Instantaneous plannar pressure determination from PIV in turbulent flow. Exp. Fluids 52 (5), 1089-1106. DOI: 10.1007/s00348-011-1237-5

Ettl, S., Kaminski, J., Knauer, M. C., H□usler, G., 2008. Shape reconstruction from gradient data. Applied Optics, 47 (12), 2091 - 2097. DOI: 10.1364/AO.47.002091

551 Gurka, R., Liberzon, A., Herfetz, D., Rubinstein, D., Shavit, U., 1999. Computation of pressure
552 distribution using PIV velocity data. In: 3rd Int. Workshop on Particle Image Velocimetry
553 (Santa Babara, USA, Sep. 16-18, 1999) 101-106.

554 Huang, H., Dabiri, D., Gharib, M., 1997. On errors of digital particle image velocimetry. Meas.
555 Sci. Technol. 8, 1427–1440. DOI: 10.1088/0957-0233/8/12/007

556 Hillier, R., Cherry, N. J., 1981. The effects of stream turbulence on separation bubbles. J. Wind
557 Eng. Ind. Aerodyn. 8 (1-2), 49–58. DOI: 10.1016/0167-6105(81)90007-6

558 Jaw, S. Y., Chen, J. H., Wu, P. C., 2009. Measurement of pressure distribution from PIV
559 experiments. Journal of Visualization. 12 (1), 27-35. DOI: 10.1007/BF03181940

560 Kiya, M., Sasaki, K., 1983. Free stream turbulence effects on a separation bubble. J. Wind Eng.
561 Ind. Aerodyn. 14 (1-3), 375–386. DOI: 10.1016/0167-6105(83)90039-9

562 Levitan, M. L., Mehta, K. C., 1992. Texas Tech field experiments for wind loads part 1:
563 building and pressure measuring system. J. Wind Eng. Ind. Aerodyn. 43 (1-3), 1565–1576.
564 DOI: 10.1016/0167-6105(92)90372-H

565 Murai, Y., Nakada, T., Suzuki, T., Yamamoto, F., 2007. Particle tracking velocimetry applied to
566 estimate the pressure field around a Savonius turbine. Meas. Sci. Techonl. 18, 2491-2503.
567 DOI: 10.1088/0957-0233/18/8/026

568 Nakamura, Y., Ozono, S., 1987. The effects of turbulence on a separated and reattaching flow.
569 J. Fluid Mech. 178, 477-490. DOI: 10.1017/S0022112087001320

570 Peren, J. I., van Hooff, T., Ramponi, R., Blocken, B., Leite, B. C. C., 2015. Impact of roof
571 geometry of an isolated leeward sawtooth roof building on cross-ventilation: Straight,
572 concave, hybrid or convex? J. Wind Eng. Ind. Aerodyn. 145, 102–114. DOI:
573 10.1016/j.jweia.2015.05.014

574 Quiroga Diaz, P. S. 2006. Uncertainty analysis of surface pressure measurements on low-rise
575 buildings. Master's thesis, The University of Western Ontario

576 Roshko, A., Lau, J. C., 1965. Some observations on transition and reattachment of a free shear
577 layer in incompressible flow. In: Proceedings of the Heat Transfer and Fluid Mechanics
578 Institute (Charwat, A. F. ed.), 157–167. Stanford/CA: Stanford University Press.

579 Saathoff, P. J., Melbourne W. H., 1997. Effects of free-stream turbulence on surface pressure
580 fluctuations in a separation bubble. J. Fluid Mech. 337, 1-24. DOI:
581 10.1017/S0022112096004594

582 Sciacchitano, A., Wieneke, B., 2016. PIV uncertainty propagation. Meas. Sci. Technol. 27,
583 084006. DOI: 10.1088/0957-0233/27/8/084006.

584 Taylor, Z. J., Gurka, R., Kopp, G. A., 2014. Effects of leading edge geometry on the vortex
585 shedding frequency of an elongated bluff body at high Reynolds numbers. J. Wind Eng.
586 Ind. Aerodyn. 128, 66–75. DOI: 10.1016/j.jweia.2014.03.007

587 Turbulent Flow Instrumentation (TFI), 2017.
588 https://www.turbulentflow.com.au/Products/CobraProbe/CobraProbe.php (Last date of
589 access: Sep. 1, 2017)

590 van Oudheusden, B. W., Scarano, F., Roosenboom, E. W. M., Casimiri, E. W. F., Souverein, L.
591 J., 2007. Evaluation of integral forces and pressure fields from planar velocimetry data for
592 incompressible and compressible flow. Exp. Fluids. 43, 153-162. DOI: 10.1007/s00348-
593 007-0261-y

594 van Oudheusden, B. W., 2013. PIV-based pressure measurement. Meas. Sci. Techonl. 24,
595 032001. DOI: 10.1088/0957-0233/24/3/032001

596 Wilcox, D. C., 2007. Basic Fluid Mechanics, Third edition. DCW Industries, Inc., USA.

597

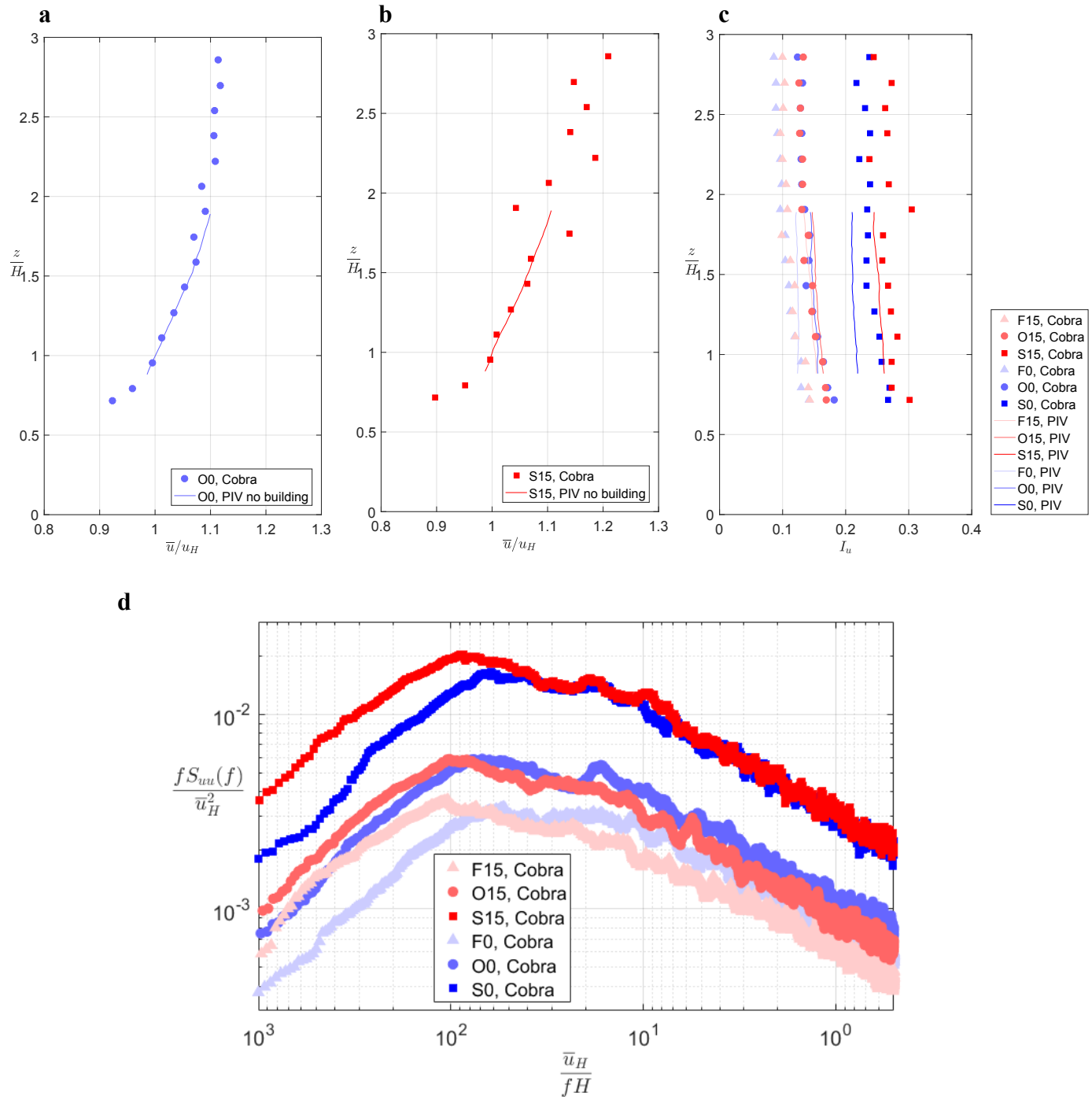

Figure 1: Mean streamwise, u, velocity for terrain (a) O0, and (b) S15 as measured by the Cobra probe and PIV, and (c) turbulence intensity profiles measured with the Cobra probe, along with (d) reduced spectral density of the streamwise velocity at roof height for the 6 terrains.

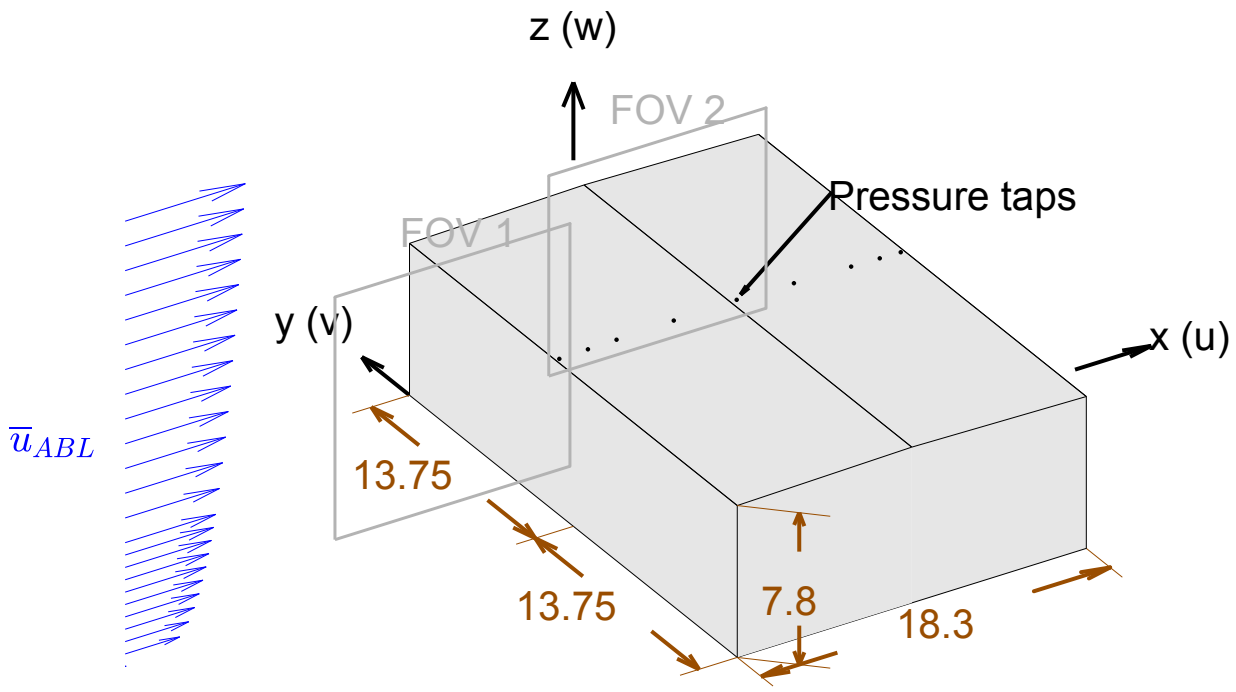

Figure 2: The low-rise building model along with planar fields of view (FOV) from the PIV measurements. The dimensions of the building model are labelled with units in centimeters. FOV-1 has a plane dimension of $\Delta x \times \Delta z = 12.3\,\text{cm} \times 12.4\,\text{cm}$, with the bottom boundary and right boundaries aligned with $z = 3.14\,\text{cm}$ and $x = -0.18\,\text{cm}$, respectively. FOV-2 has a plane dimension of $\Delta x \times \Delta z = 11.4\,\text{cm} \times 10.3\,\text{cm}$, with the bottom boundary and left boundaries aligned with $z = 8.11\,\text{cm}$ and $x = -1.29\,\text{cm}$, respectively.

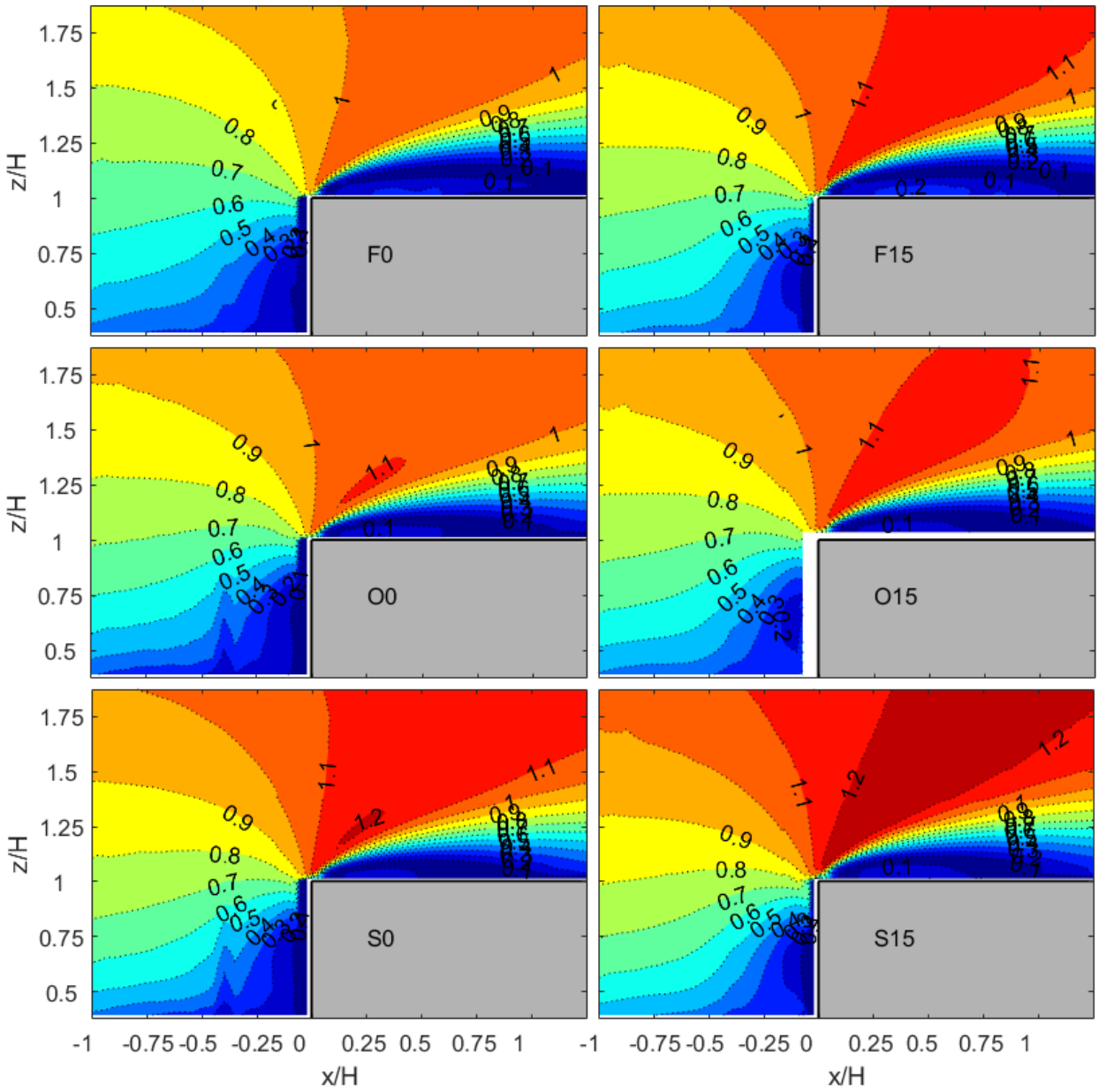

Figure 3: Mean velocity ratio, $|\overline{\mathbf{u}}|/u_{ref}$, near the roof obtained for the six terrains.

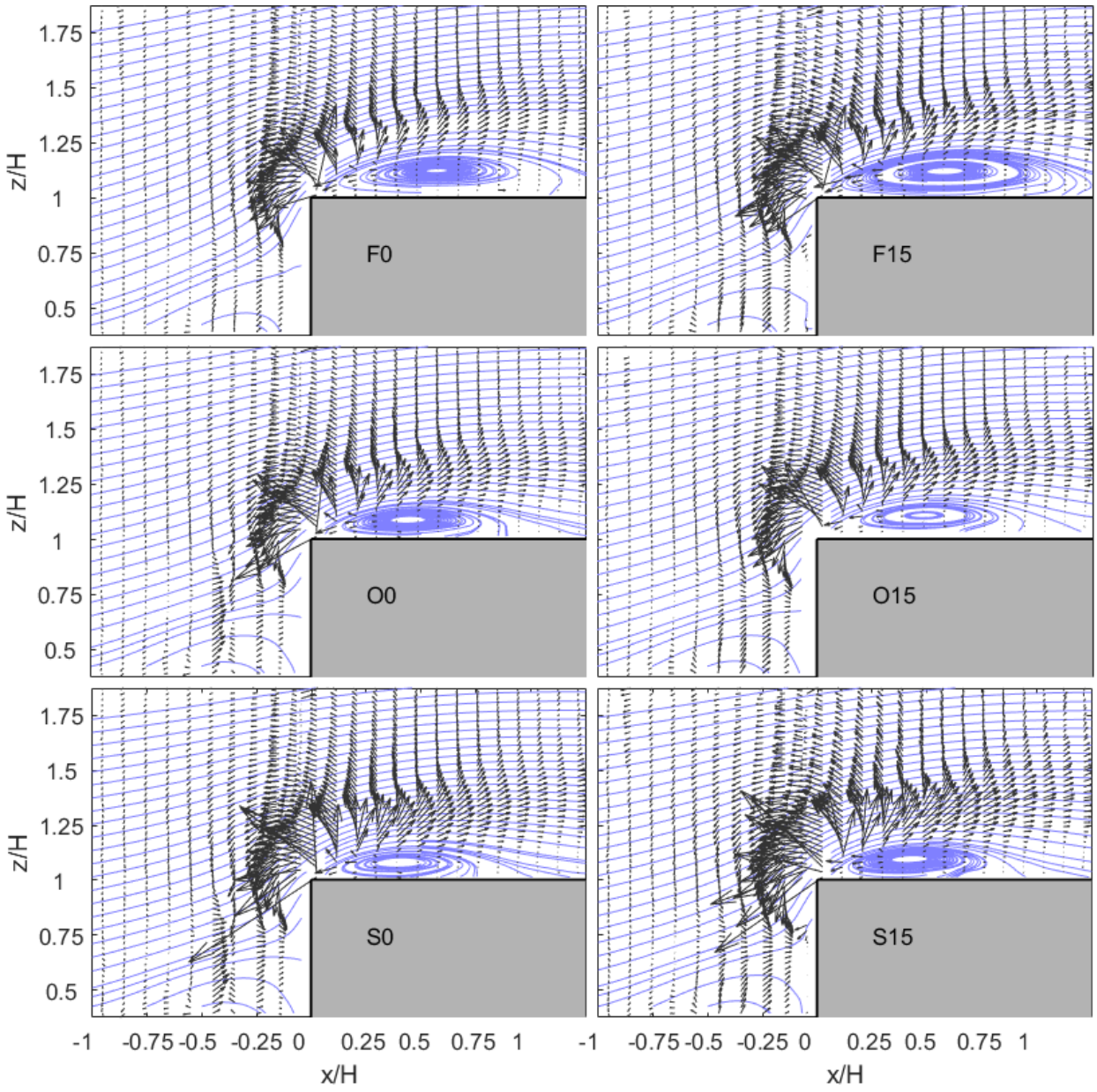

Figure 4: Pressure gradient vectors for the mean convection term in the Navier-Stokes equations for the six terrains, along with streamlines. (Note that only one of every four vectors is shown in the x-direction.)

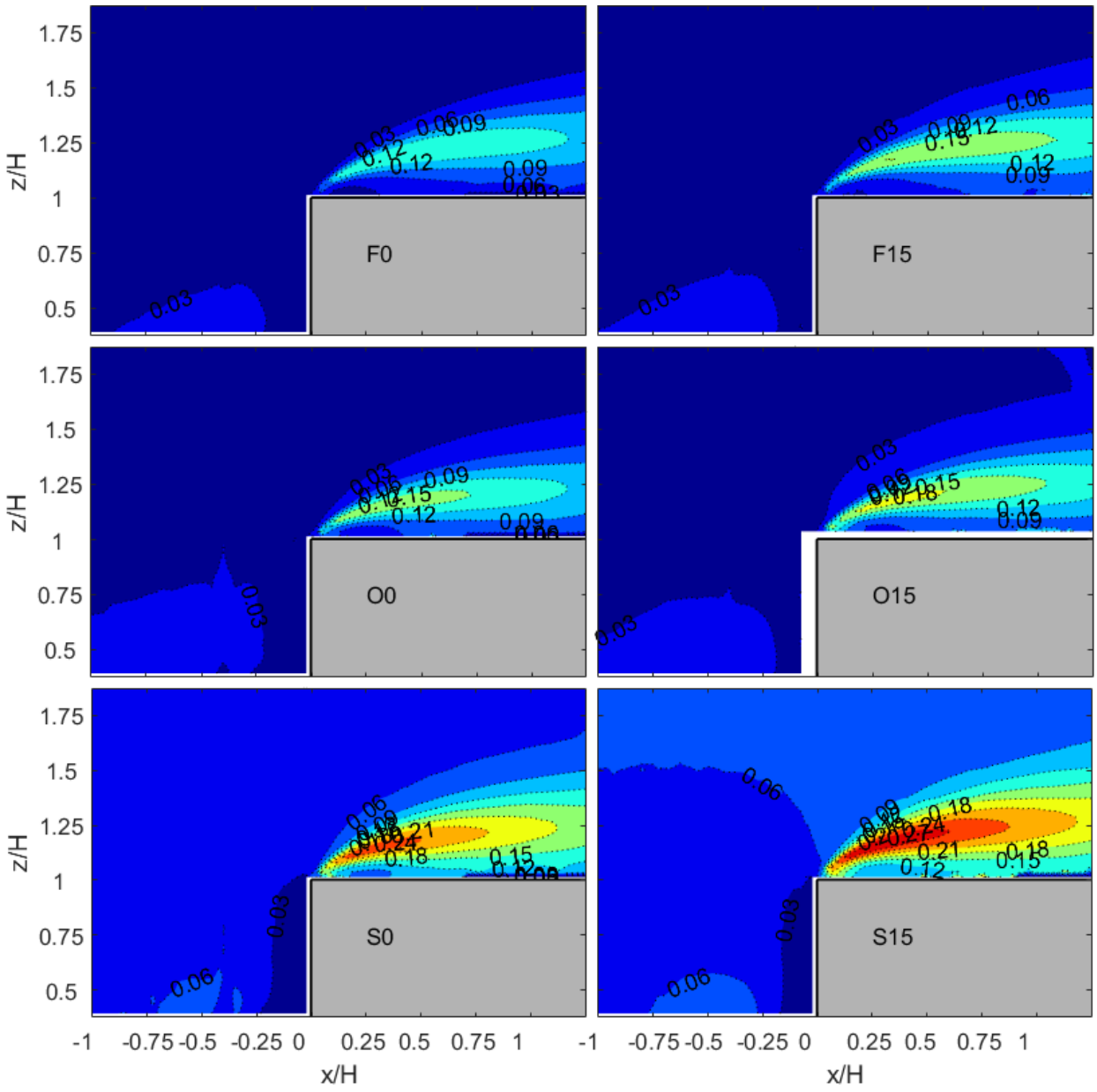

Figure 5: Streamwise Reynolds normal stresses, $\overline{u'u'}/u_{ref}^2$, for the six terrains.

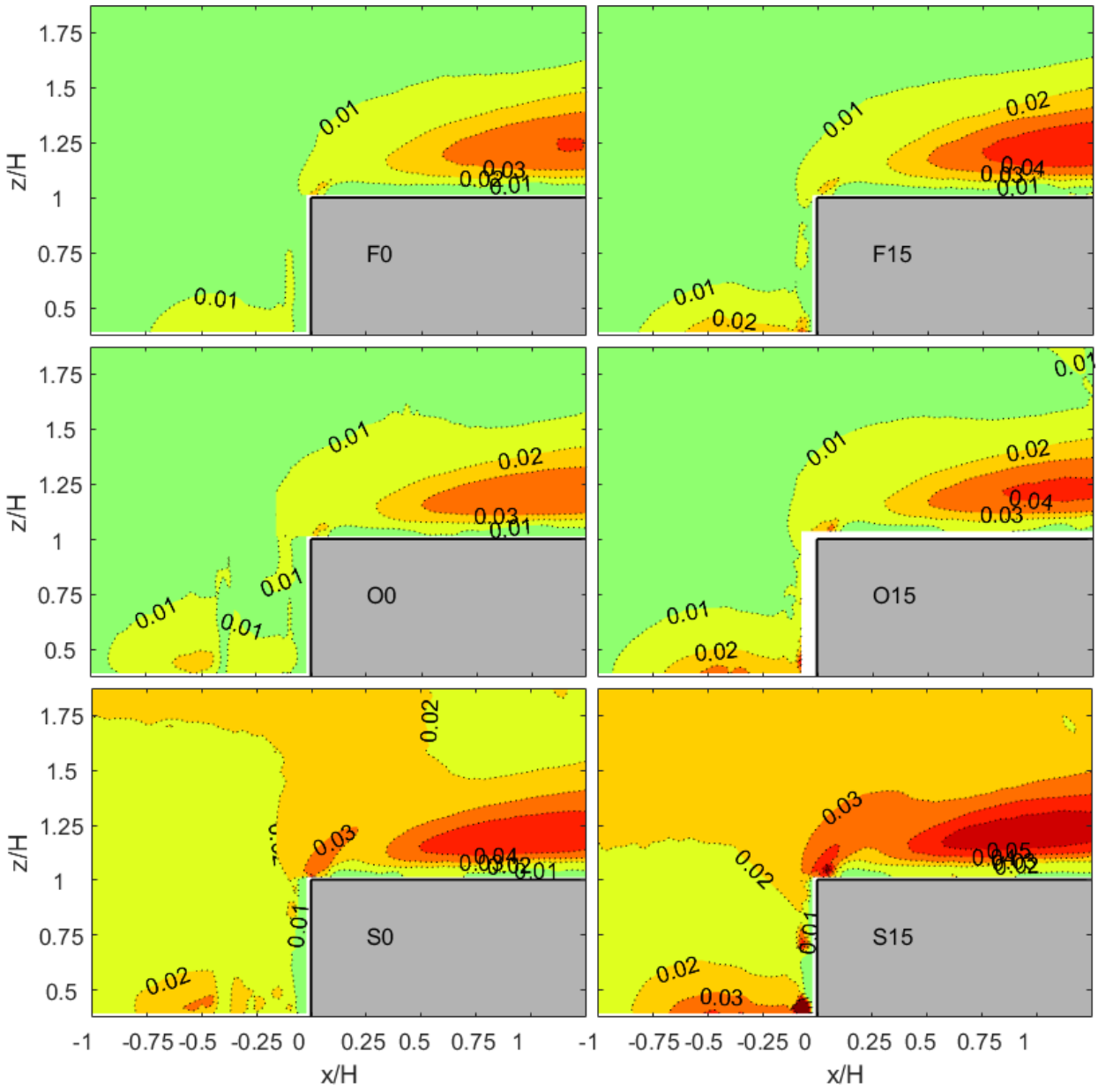

Figure 6: Vertical Reynolds normal stresses, $\overline{w'w'}/u_{ref}^2$, for the six terrains.

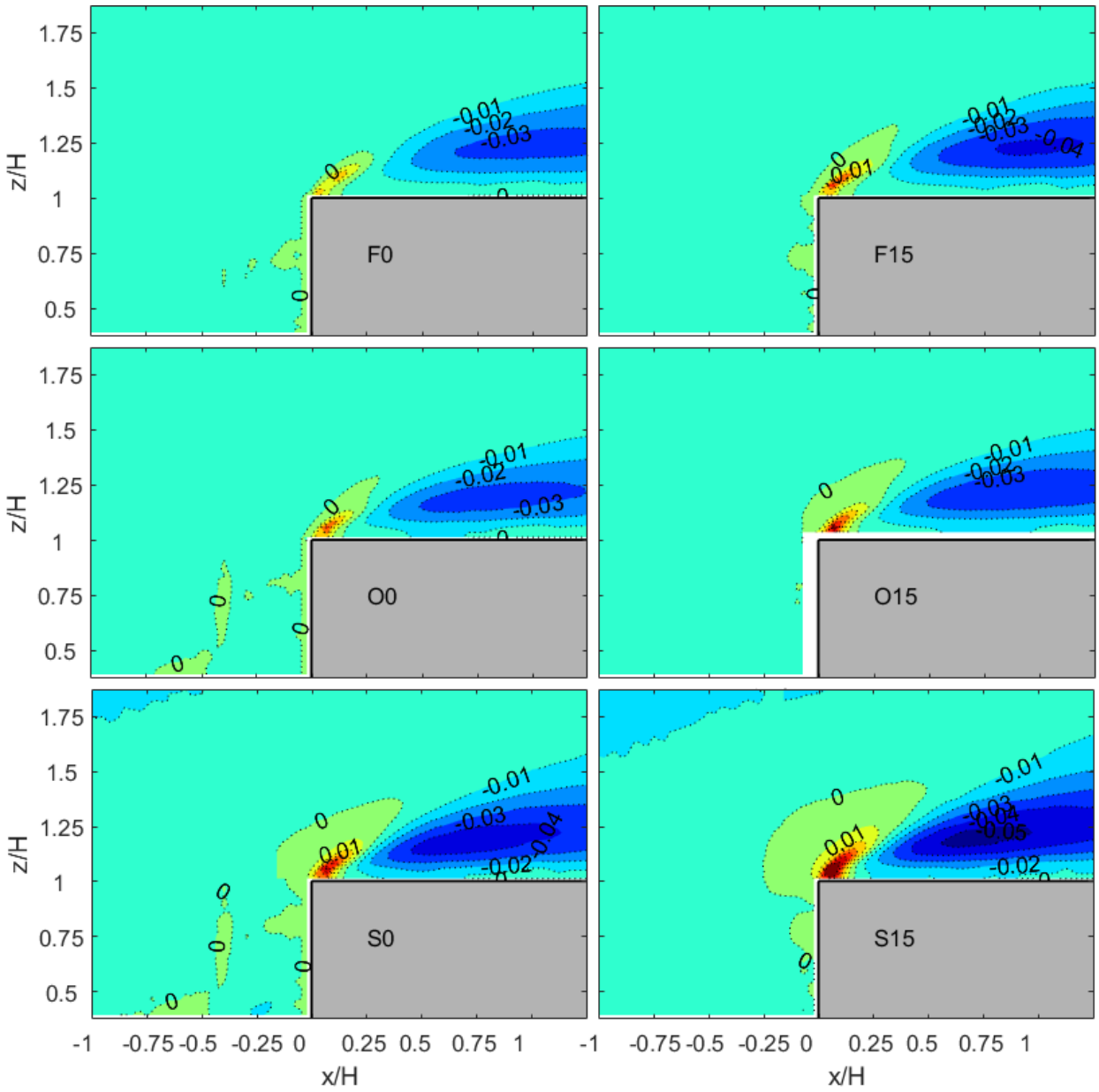

Figure 7: Reynolds shear stresses, $\overline{u'w'}/u_{ref}^2$, for the six terrains.

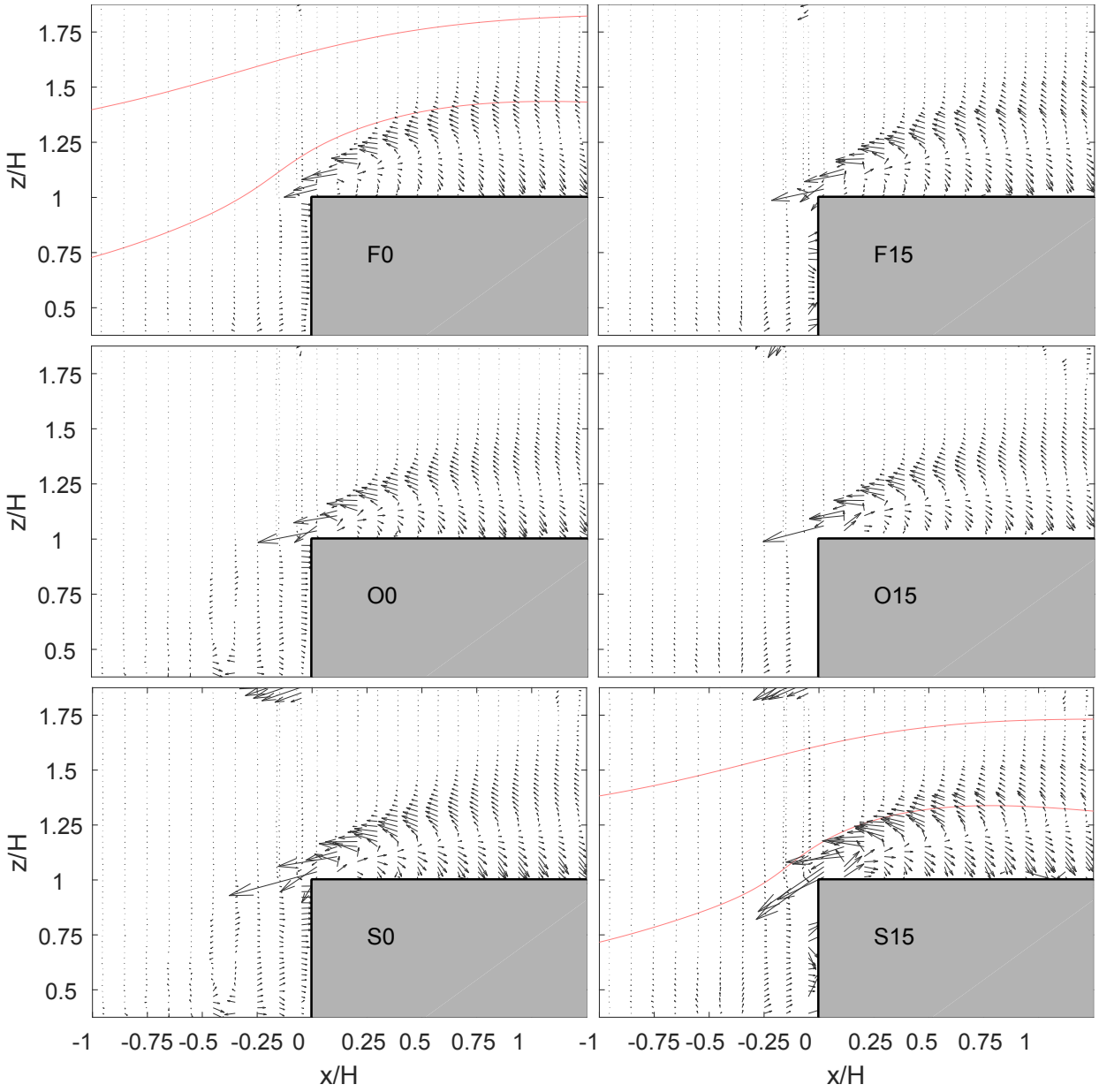

Figure 8: Pressure gradient vectors for the turbulence term in the Navier-Stokes equations for the six terrains. (Note that only one of every four vectors is shown in the x-direction.)

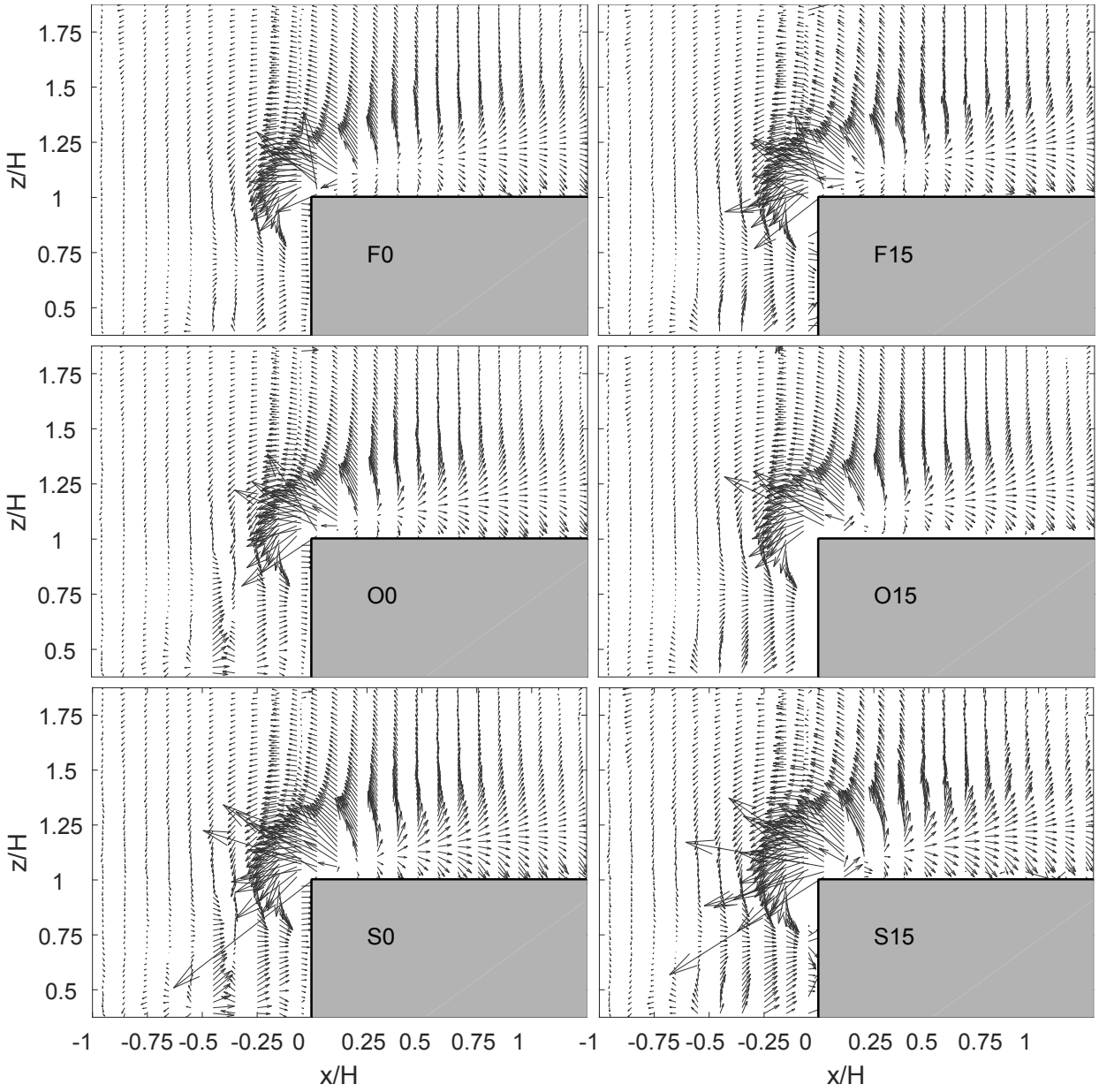

Figure 9: The total pressure gradient vectors for the six terrains. (Note that only one of every four vectors is shown in the x-direction.)

a

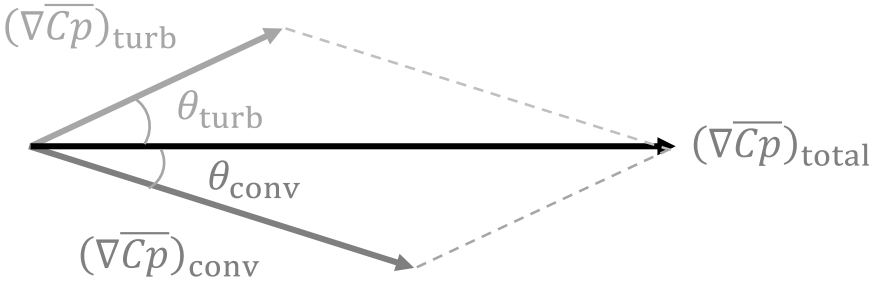

b

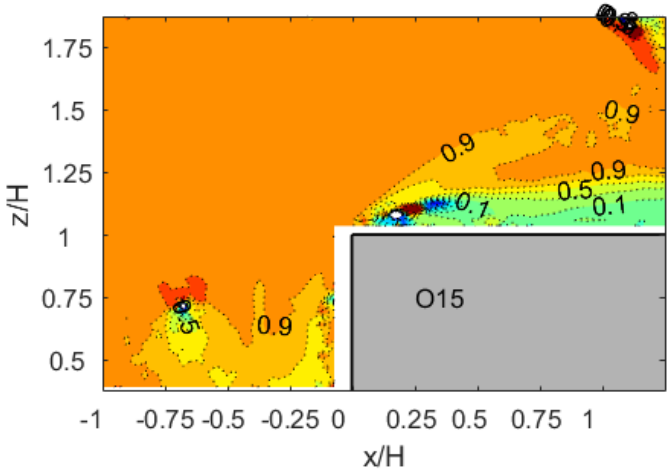

c

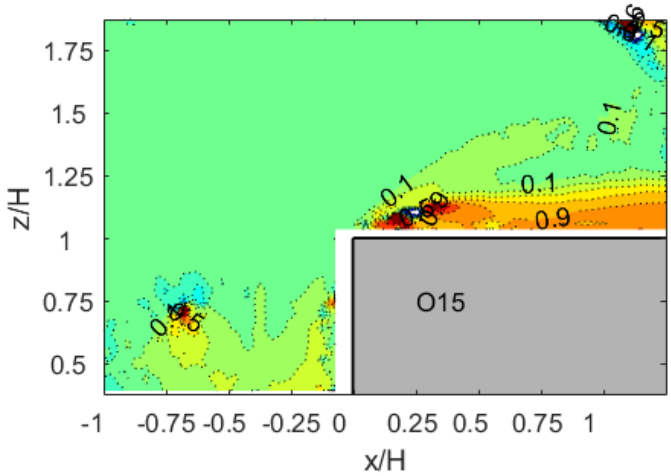

Figure 10: (a) Schematic of total pressure gradient vector at a point, along with the contours of the contributions of the (b) convection and (c) turbulence terms for the terrain, O15.

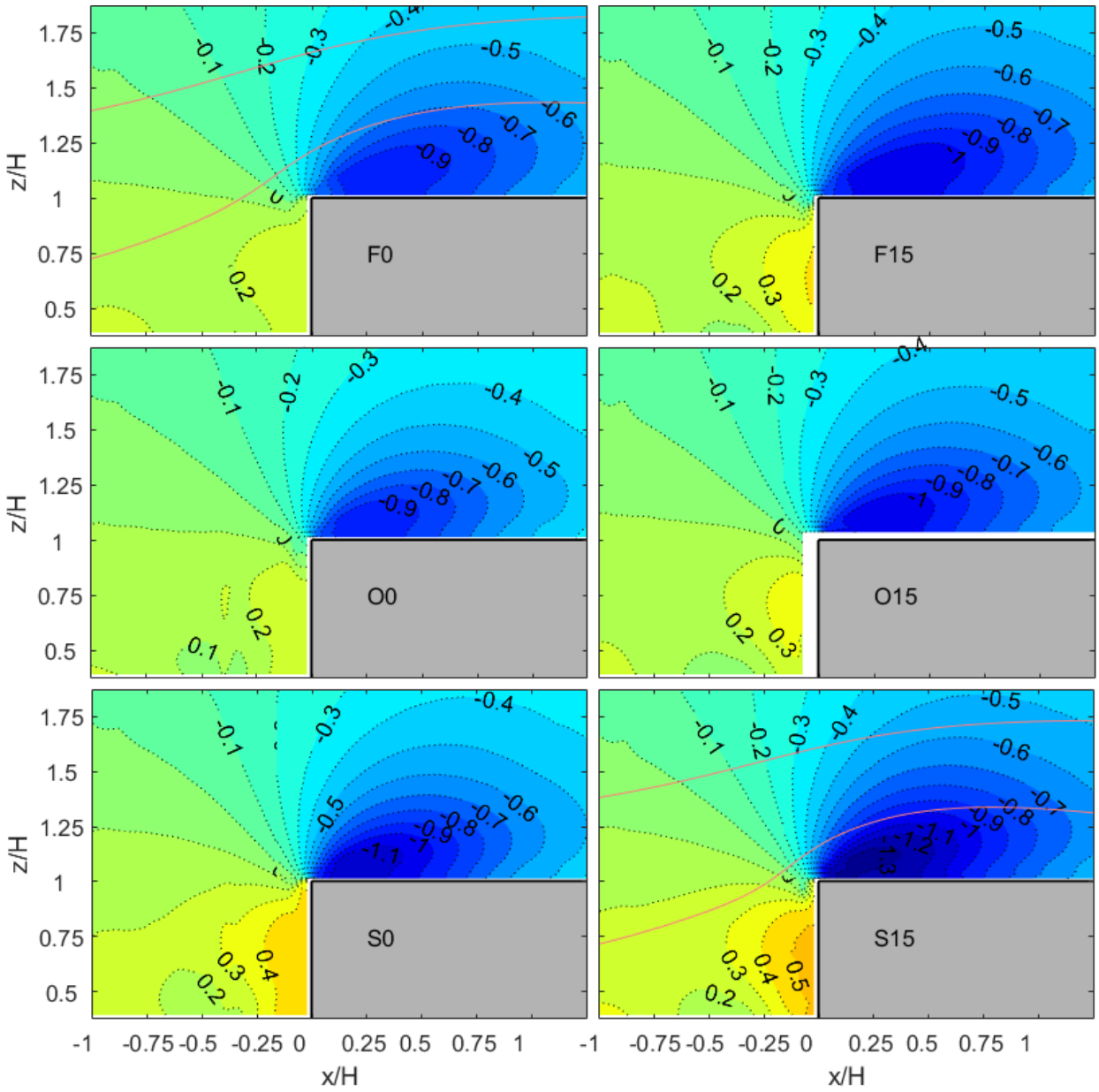

Figure 11: The mean pressure, $\overline{Cp}$, fields obtained using the analytical interpolation technique for the six terrains.

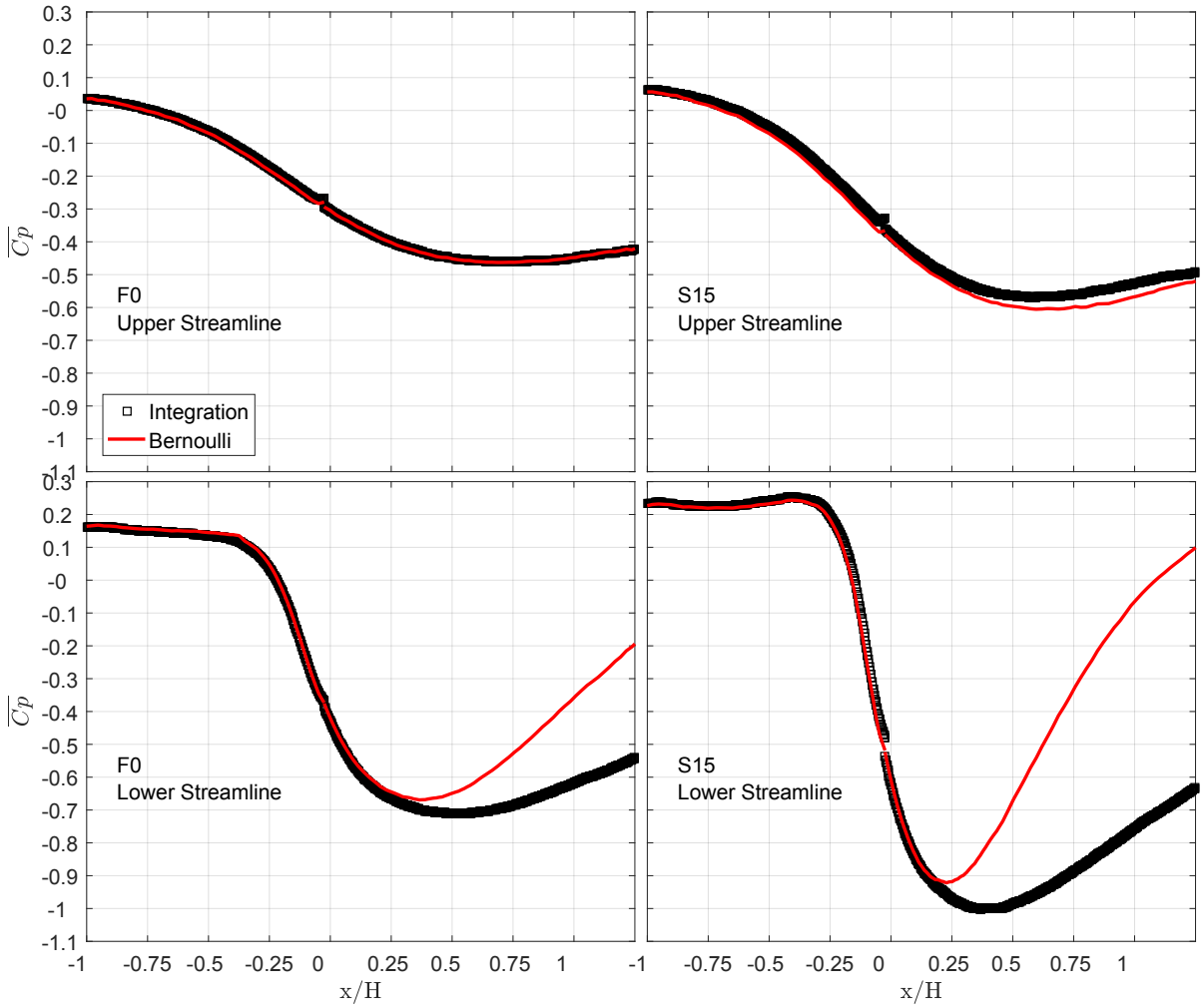

Figure 12: The mean pressure, $\overline{Cp}$, obtained from the analytical interpolation technique and from Bernoulli's equation along upper and lower streamlines in terrains 'F0' and 'S15'.

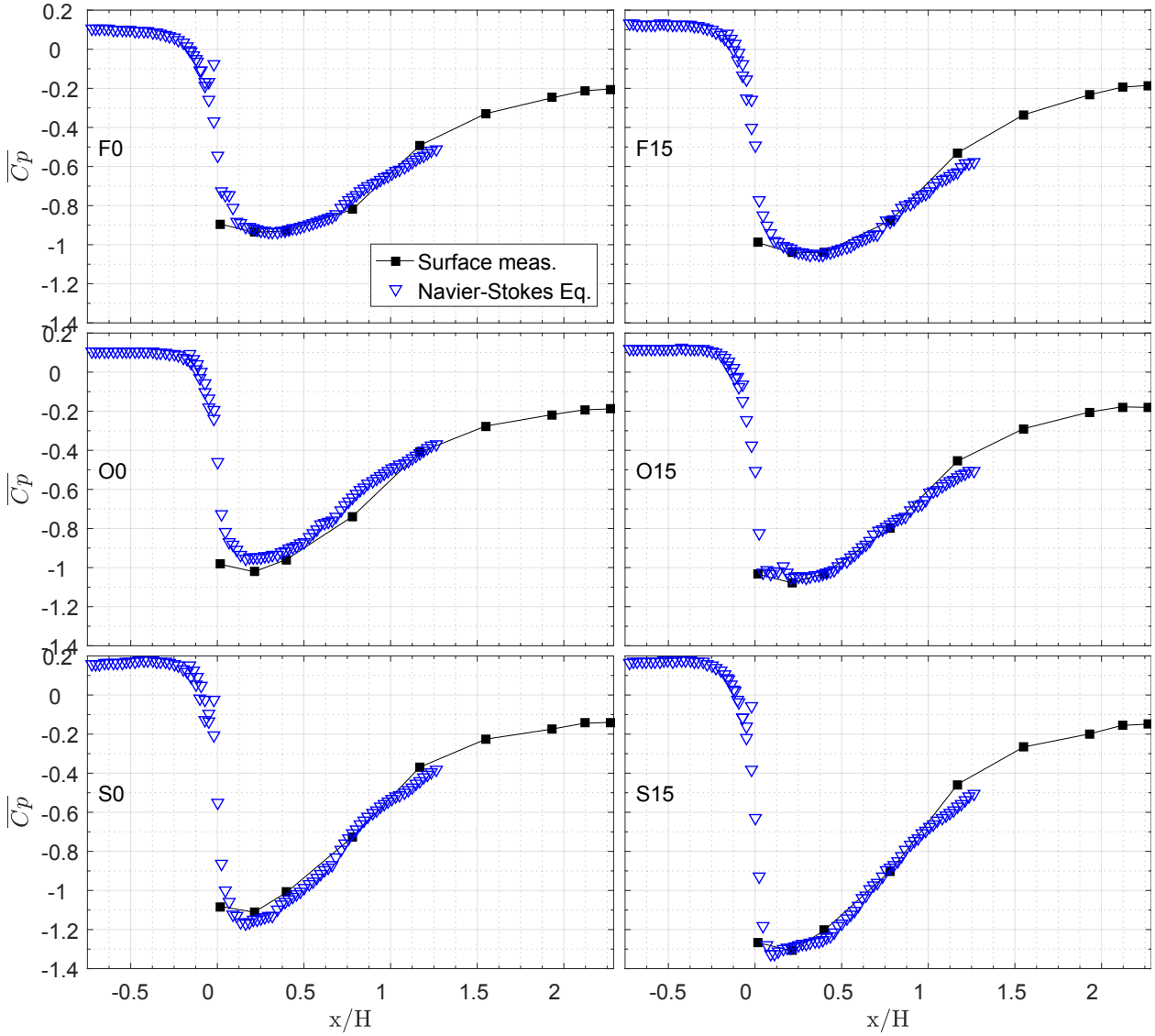

Figure 13: Mean pressure coefficients on the roof surface, $\overline{Cp}$, obtained from measurements and the analytical interpolation technique for the six terrains.

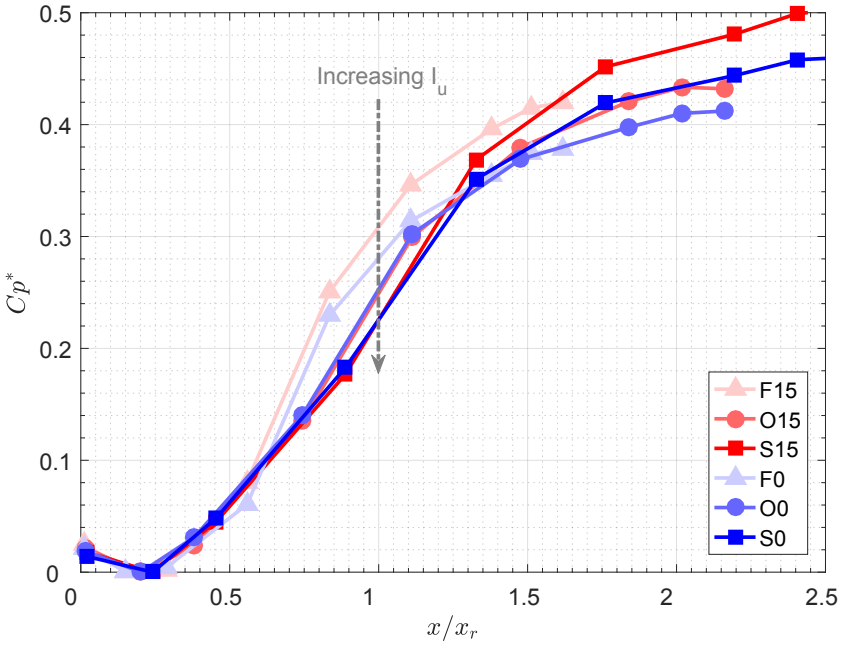

Figure 14: Reduced pressure coefficient Cp* obtained from surface pressure measurements for the six terrains (Akon and Kopp, 2016).